Prediction of Ankle Dorsiflexion Moment by Combined Ultrasound Sonography and Electromyography

Qiang Zhang, Kang Kim*, and Nitin Sharma*

***Abstract*—To provide an effective and safe therapy to persons with neurological impairments, accurate determination of their residual volitional ability is required. However, accurate measurement of the volitional ability, through non-invasive means (e.g., electromyography), is challenging due to signal interference from neighboring muscles or stimulation artifacts caused by functional electrical stimulation (FES). In this work, a new model-based intention detection method that combines signals from both surface electromyography (sEMG) and ultrasound (US) sonography to predict isometric volitional ankle dorsiflexion moment is proposed. The work is motivated by the fact that the US-derived signals, unlike sEMG, provide direct visualization of the muscle activity, and hence may enhance the prediction accuracy of the volitional ability, when combined with sEMG. The weighted summation of sEMG and US imaging signals, measured on the tibialis anterior muscle, is utilized as an input to a modified Hill-type neuromusculoskeletal model that predicts the ankle dorsiflexion moment. The effectiveness of the proposed model-based moment prediction method is validated by comparing the predicted and the measured ankle joint moments. The new modeling method has a better prediction accuracy compared to a prediction model that uses sole sEMG or sole US sonography. This finding provides a more accurate approach to detect movement intent in the lower limbs. The approach can be potentially beneficial for the development of US sonography-based robotic or FES-assisted rehabilitation devices.**

***Index Terms*—Ankle dorsiflexion, Voluntary contraction force, Ultrasound sonography, Electromyography, Pennation angle, Muscle fascicle, Neuromusculoskeletal model**

I. Introduction

Robotic rehabilitation or functional electrical stimulation (FES)-based therapy often uses knowledge of a person's residual volitional ability to determine compensation torque or force such as during assist-as-needed therapy [1]–[3]. To predict the volitional ability, both mechanical and neuromuscular sensors have been implemented. Mechanical sensors measure physical human-machine-interaction (pHMI) directly. For example, several types of compliant actuators [4], [5] have been developed that use embedded elastic elements for detecting interaction forces. However, installation of mechanical sensors relies on a rigid and bulky structure, which limits the portability of the devices. In addition, inaccuracies can creep in because the powered exoskeleton frames are prone to human-robot misalignment that can induce undesired interaction forces [6]–[8]. Neuromuscular sensors approaches, such as surface electromyography (sEMG), have also been proposed to identify user's movement intent [9]. sEMG signals are combined muscle potentials that act as surrogates to neural signals that originate from the central nervous system. A major challenge that limits the implementation of neuromuscular sensors to predict human movement intent is the difficulty to bridge the connection between events taking place at the neurophysiological level (i.e. neural signals descending from the spinal cord) with those at the musculoskeletal level (i.e. muscle contraction force or joint moment) [10]. Two methodologies, a model-free approach and a model-based approach, aim to bridge the relationships between the neuromuscular signals and mechanical functions of human limbs. In the model-free approach [11]–[13], given the experimental observations of the variables, a machine learning approximation is utilized to establish a numerical function that maps different variables, such as from sEMG to joint moment or joint angle. These mapping functions can be approximated by the combination of basis functions, e.g., linear or nonlinear polynomials [14], exponential and Gaussian functions [12], [15], as well as linear and nonlinear regression [13] between neural signals and skeletal mechanical functions. Artificial neural network (ANN) is another model-free approach that can also be used to map the relationship between the above variables. For example, in [16], [17] ANN-based relationship was established between sEMG signals to tendon force in the cat soleus and gastrocnemius muscles and in [18] a relationship between sEMG signals to joint moments and joint angles during human locomotion was determined. Although sEMG sensors are readily available and can be implemented with fair ease, they cannot reliably detect human intention due to their susceptibility to signal interference coming from neighboring muscles. Moreover, it cannot be used to detect contractions of deeply-located muscles [19]. Ultrasound (US) imaging is another non-invasive methodology that addresses sEMG's drawbacks, and can be potentially used for muscle effort

Qiang Zhang and Nitin Sharma are with the UNC & NC State Joint Department of Biomedical Engineering, NC State University, Raleigh, NC, USA. (e-mail: qzhang25@ncsu.edu and nsharm23@ncsu.edu).

Kang Kim is with the Department of Bioengineering, University of Pittsburgh School of Engineering, Pittsburgh, PA, USA. (e-mail: kangkim@upmc.edu). Kang Kim is also with the Center for Ultrasound Molecular Imaging and Therapeutics-Department of Medicine and Heart and Vascular Institute, University of Pittsburgh School of Medicine and University of Pittsburgh Medical Center, Pittsburgh, PA, USA. Kang Kim is also with the Department of Mechanical Engineering and Materials Science, University of Pittsburgh School of Engineering, Pittsburgh, PA, USA. Kang Kim is also with the McGowan Institute for Regenerative Medicine, University of Pittsburgh and University of Pittsburgh Medical Center, Pittsburgh, PA, USA. (*Co-corresponding authors: Kang Kim and Nitin Sharma)

This work was funded by NSF CAREER Award # 1750748.

and joint moment prediction. The architectural parameters of muscle's US images can reliably provide changes in muscle contractility of a deeply located muscle without cross-talk or interference from the adjacent muscles. The relationship between architectural parameters (including pennation angle (PA), fascicle length, and muscle thickness) and joint mechanical function has been also addressed by aforementioned model-free approaches. For example, in [12], the exponential functions between the normalized muscle deformation and the normalized sEMG's root mean square (RMS), and the normalized PA and the normalized sEMG's RMS were observed. In addition, the linear relationships between the normalized muscle deformation and torque, as well as the normalized PA and torque were observed.

However, the model-free approach is essentially a black box approach, where all intermediate functional relationships between experimental variables are not explicitly identified. Thus, its main limitation is that the knowledge that contributes to the understanding of mechanisms underlying the experimental variables may remain unknown. To establish a direct cause-effect mapping across those variables, a model-based approach, e.g., a Hill-type neuromusculoskeletal model (HNM), has been exploited to analytically define the functional relationship between the measured neuromuscular signals and skeletal mechanical functions [20]–[22]. An HNM usually contains the following modules: neural activation, muscle activation, musculoskeletal geometry, and skeletal dynamics [23]. sEMG along with advanced processing techniques can experimentally access the neural information from muscles contractions [24]. Thus, sEMG-based estimation of neuromuscular excitation has been utilized to drive the HNM during a variety of human dynamic motor functionalities, like in [25], [26]. In addition, it can predict muscle forces [27], joint moments [26], [28], joint compressive forces [29], [30], joint stiffness [31], [32] and joint angles [33]. Although the model-based approach can indicate the intermediate mechanisms between neuromuscular variables and skeletal functions, it is directly limited by the uncertainties arising from the unmeasured physiological parameters, such as fiber length, tendon length, PA, and so on. The simulation approximation of those parameters was studied in [20], [21], [34], where given the weight, height, and limb length of the participants, the non-subjective physiological parameters were roughly approximated offline by using the OpenSim software.

As aforementioned, although the feasibility of HNM in musculoskeletal mechanical functions has been verified and popularly applied, most studies only considered the EMG-induced muscle activation. Few studies have incorporated the architectural parameters of the targeted muscle to the muscle contraction in an HNM. In addition, the approximated offline physiological parameters from the OpenSim software can hardly reflect the real-time neuromuscular conditions of an individual participant. In our recent work [13], PA information derived from US images was supplemented with sEMG signals by determining the optimal allocation coefficient to improve accuracy in human intention detection. Based on that work, the idea is extended to the model-based approach, where an optimal combination of sEMG signal and US imaging-derived

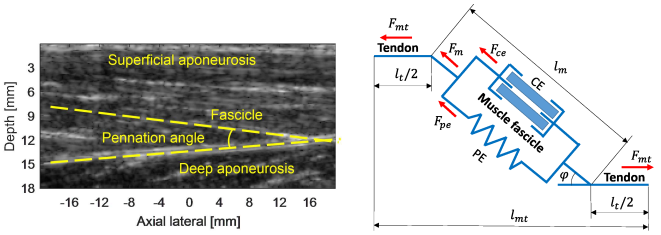

(a) (b)

Figure 1: (a) A US image of the TA muscle. (b) Schematic of the Hill-type muscle-tendon model.

PA information is used as an input to the HNM. Then, like mentioned in [22], during the muscle contraction dynamic procedure, muscle physiological parameters including fascicle length, fascicle velocity, and PA are extracted from US images by using a commercial muscle fascicle tracking algorithm [35], [36], that enables a potential real-time implementation. The objective of this work is to investigate the feasibility of the proposed HNM, considering both sEMG and PA information in muscle activation dynamics, and to evaluate the ankle moment prediction performance compared to the HNM that takes only sEMG-induced or PA-induced factor in the muscle activation dynamics.

II. HNM for Ankle Moment Prediction

Given the human physiological and anatomical parameters, HNM is an efficient computational method to simulate the muscle contraction force and corresponding joint torque [37]. Three main parts in the modified HNM are proposed : (1) musculoskeletal geometry model, (2) sEMG and PA-to-activation model, and (3) muscle contraction dynamics model.

A. Musculoskeletal Geometry Model

The musculoskeletal geometry model depicted in Fig. 1 (b) can be measured from US images, shown in Fig. 1 (a). $l_{mt} \in \mathbb{R}^+$ is a muscle-tendon unit's length, $l_t \in \mathbb{R}^+$ is a length of a tendon, $l_m \in \mathbb{R}^+$ is a length of a muscle fascicle, and $\varphi \in \mathbb{R}^+$ is the PA defined in Fig. 1 (a). The PA was the summation of two parts [13], one is the angle between the visualized fascicle and horizontal line, and the other one is the angle between the deep aponeurosis and horizontal line.

B. sEMG and PA-to-Activation Model

The sEMG and PA-to-activation model represents the level of muscle activation by synthesizing an sEMG signal and PA information. To use the sEMG signal and the PA signal, as inputs to the model, the MRMS of a band-pass filtered sEMG signal and PA are normalized with respect to the peak MRMS value and the peak PA value, which are recorded corresponding to the maximum voluntary isometric contraction (MVIC), respectively. As mentioned in [13], there exists a delay between the onsets of an sEMG signal and a muscle contraction, which is known as an electromechanical delay (EMD) and is determined by experimental results. Taking this

into consideration, a second-order recursive filter was proposed to calculate the neural activation $u(t)$ from the processed sEMG signal $N_1(t)$ in [37]

$$u(t) = \alpha N_1(t-\tau) - \beta_1 u(t-1) - \beta_2 u(t-2) \quad (1)$$

where α = 0.9486, β_1 = -0.056, and β_2 = 0.000627 [37]. N_1 and $\tau \in \mathbb{R}^+$ are the pre-processed sEMG signal and the EMD, respectively. According to [38], when the muscle activation is at a low level, there is a nonlinear relationship between the neural activation and the muscle activation, so a one-parameter segmented transfer model from the neural activation $u(t)$ to the sEMG-induced muscle activation $a_1(t)$ is given as

$$\begin{cases} a_1(t) = d\ln(cu(t)+1), 0 \le u(t) < u_0 \\ a_1(t) = mu(t) + b, u_0 \le u(t) < 1 \end{cases}. \quad (2)$$

The point (u_0, a_{10}) of the nonlinear model is defined as

$$\begin{cases} u_0 = 0.3085 - A\cos(45^\circ) \\ a_{10} = 0.3085 + A\sin(45^\circ) \end{cases}. \quad (3)$$

Knowing that the linear portion of the curve in (2) must pass through two points (u_0, a_{10}) and (1,1), then the coefficients m and b in (2) can be determined as $m = \frac{1-a_{10}}{1-u_0}$ and $b = \frac{a_{10}-u_0}{1-u_0}$. The coefficients d and c in (2) can be determined by making the nonlinear portion pass through point (u_0, a_{10}), then $c = \frac{e^{\frac{a_{10}}{d}}-1}{u_0}$, and d is calculated iteratively by using the Newton-Raphson method. Therefore, the four parameters d, c, m and b are all strongly related to the point (u_0, a_{10}), which is determined by shape coefficient A in (3). In addition, A was reported within the range from 0 to 0.12 [38], which is to be determined by system identification.

Similarly, neglecting the time delay between PA and muscle activation, the PA-induced muscle activation $a_2(t)$ is assumed to be equivalent to the pre-processed PA $N_2(t)$, which is represented by $a_2(t) = N_2(t)$. Thus, in this work, the linearly synthesized muscle activation $a(t)$ is defined as

$$a(t) = \delta a_1(t) + (1-\delta)a_2(t) \quad (4)$$

where δ is an allocation coefficient that needs to be optimized. The pre-processed sEMG signal $N_1(t)$ and PA information $N_2(t)$ are discussed in the experiments section.

C. Muscle Contraction Dynamics

The moment produced by the isometric ankle dorsiflexion is the product of the TA tendon force and the moment arm:

$$M_{predict}(t) = F_{mt}(t) r_{mt}(q) \quad (5)$$

where $r_{mt} \in \mathbb{R}^+$ denotes the moment arm of muscle tendon force [39] and is defined as $r_{mt} = c_1 e^{-2q^2}\sin(q) + c_2$, where positive constants c_1 and c_2 for individual participant are identified from experimental data. q is the ankle angular position corresponding to neutral position (neither dorsiflexion nor plantar flexion). F_{mt} denotes the force generated by the muscle-tendon unit:

$$F_{mt}(t) = F_m(t)\cos(\varphi(t)) = (F_{ce}(t) + F_{pe}(t))\cos(\varphi(t)) \quad (6)$$

where F_{ce} and F_{pe} denote the force generated by the contractile element and the passive elastic element. The calculation of F_{ce} and F_{pe} are given by

$$\begin{cases} F_{ce}(t) = f(l_m(t))f(v_m(t))a(t)F_{mx} \\ F_{pe}(t) = f_p(l_m(t))F_{mx} \end{cases} \quad (7)$$

where F_{mx} represents the muscle-tendon force at MVIC, $f(l_m)$ represents the generic force-fiber length relationship for the contractile element (CE), $f(v_m)$ represents the generic force-fiber velocity relationship for CE [40], and $f_p(l_m)$ represents the generic force-fiber length relationship for the passive elastic element (PE). These functions are defined as

$$f(l_m) = e^{-\left(\frac{1}{b_1}(\sigma_l - 1)\right)^2} \quad (8)$$

$$f(v_m) = \begin{cases} \frac{0.3(\sigma_v+1)}{-\sigma_v+0.3}, & (\sigma_v < 0) \\ \frac{2.34\sigma_v+0.039}{1.3\sigma_v+0.039}, & (\sigma_v \ge 0) \end{cases} \quad (9)$$

$$f_p(l_m) = 0.129\left(e^{4.525(\sigma_l-1)} - 1\right) \quad (10)$$

where b_1 is an unknown subjective constant to be identified. $\sigma_l = \frac{l_m}{l_{mo}}$ is the ratio between fascicle length and optimal fascicle length associated with muscle activation a, and the optimal fascicle length is given as $l_{mo} = l_o(\lambda(1-a)+1)$, where λ is the rate of change in the optimal fascicle length, and it has been reported as 0.15 in [37]. $\sigma_v = \frac{v_m}{l_{mo}}$ is muscle fascicle contraction velocity (known as time derivative of l_m) normalized to l_{mo}.

During ankle isometric dorsiflexion, the angular position of the ankle joint is kept constant. The measurement from a load cell is the pull force F_l that is perpendicular to the pedal, so the measured ankle joint moment does not rely on q, which is given as

$$M_l(t) = F_l(t) r_l \quad (11)$$

where r_l is the constant distance from the attachment point of the load cell to the rotation center of the ankle joint.

Remaining unknown modeling parameters identification, including A, δ, c_1, c_2, and b_1 are found by using the Least Squares Method. The Matlab function $lqscurvefit$ was used to minimize the squared error equation:

$$Error = \frac{1}{N}\sum_{i=1}^{N}\left(M_{predict}(i) - M_l(i)\right)^2 \quad (12)$$

where N represents the length of the collected data, $M_{predict}$ is the dorsiflexion moment established based on HNM, and M_l is the real moment is measured by load cell. All other parameters in the above formulations N_1, N_2, l_o, l_m, φ_0, φ, and F_{mx} are obtained from the sEMG signals, US images, and load cell signals. It is assumed that the TA muscle is an autonomous system during a short time voluntary contraction, and its mechanical characteristics remain time-invariant.

III. Experiments

A. Participants

This study was approved by the Institutional Review Board (IRB) at the University of Pittsburgh (IRB approval number: PRO18020072). All participants signed an informed consent

form. Inclusion criteria were persons of age of 18-40 years old, without any neuromuscular disorders, and able to perform ankle movements such as planar flexion, dorsiflexion, eversion and inversion, and able to sit patiently. Exclusion criteria were: 1. any difficulty or an orthopedic condition that would impede ankle movements such as planar flexion, dorsiflexion, eversion and inversion, 2. absent sensation in lower extremities, and 3. allergy to adhesive skin tapes and/or ultrasound gels. Four participants were involved in this study. Participant 1: Age 24, male. Participant 2: Age 25, male. Participant 3: Age 27, male. Participant 4: Age 22, male.

B. Ankle Experimental Scenarios

The experimental setup of this study is illustrated in Fig. 2 (a), where the participant was seated comfortably in an adjustable chair with his upper leg kept horizontal. During the entire experiment time, the participant's lower leg was restrained perpendicular to the upper leg. A region that is around 10 cm away from the rotation center of the knee joint was chosen as a targeted area. The sEMG sensor in Fig. 2 (b) (Bagnoli^{TM} Desktop, DELSYS, MA, USA) was attached to the lower leg skin through a piece of adhesive interface after shaving and cleaning with alcohol in the targeted area. A clinical linear US transducer (L7.5SC Prodigy Probe, S-Sharp, Taiwan) was pressed onto the targeted muscle of the lower leg with a special customized holder as shown in Fig. 2 (c). This holder with 1 degree of freedom was 3-D printed, and can orient the US probe in cross-sectional direction or in longitudinal direction to maximize a visualization of the targeted muscle area. Conductive US gel was applied between the transducer and the skin. The transducer was placed to image a longitudinal direction instead of a cross-sectional direction. In this direction, inaccurate measurements caused by muscle fibers moving out of the imaging window can be avoided. The load cell platform is shown in Fig. 2 (d), which includes base frame, adjustable angular positions, pedal, and load cell (MLP-300, Transducer Techniques, CA, USA). The angular positions of the pedal could be set as -15°, -10°, -5°, 0°, 5°, 10°, and 15° corresponding to the ground, which means that there are 7 experimental scenarios for each participant. For the initial angular position 0°, known as the neutral position, the pedal of the platform was set to be parallel to the ground. As shown in Fig. 2 (a), both the heel and toe of the participant's foot were tied to the pedal tightly by velcro straps to guarantee the isometric ankle dorsiflexion. The load cell in Fig. 2 (d) was located beneath the pedal to measure the equivalent voluntary contraction force (VC) of the dorsiflexor muscle group during ankle dorsiflexion. For the isometric case, the moment arm during VC was kept as a constant, and the ankle torque was computed by multiplying VC and the moment arm.

The 7 scenarios were conducted in the following order as 0°, -5°, -10°, -15°, 5°, 10° and 15°. In each scenario, there were two sets experiments. In the first set, three repeated trials of MVIC maintaining 2 seconds were separately performed by the participants to determine the ankle joint moment, sEMG signal and US image at MVIC. Then in the second

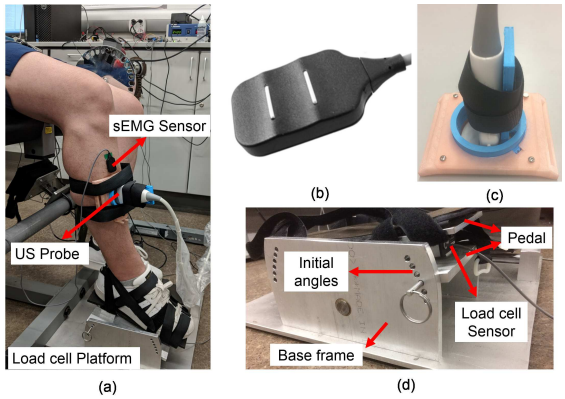

Figure 2: (a) The experimental setup used to simultaneously record sEMG, US imaging, and load cell signals during the ankle dorsiflexion. (b) Single differential sEMG sensor. (c) 3-D printed customized US probe holder with 1 degree of freedom. (d) Load cell platform with 7 adjustable angular positions.

set, there were also three trials in each scenario, and the duration for each trial lasted 7 seconds with the 1^{st} second left intentionally blank to get every signal channel ready for receiving data. After 1^{st} second, the participants performed dorsiflexion. The movement was repeated twice within 6 seconds, and the movement sequence included a relaxation period, gradual contraction to MVIC, and relaxation period again. The instructions to perform the sequence was given orally. Totally there were six dorsiflexion cycles for three trials in the second set experiments in each scenario per participant. To avoid fatiguing the muscle, a rest period of 2 minutes to 4 minutes between two successive trials was provided.

C. Data Acquisition and Pre-processing

The signal from the load cell was processed through an input signal conditioner (DRC-4710, OMEGA Engineering, CT, USA), which amplified the original signal and filtered the noise. The signal from the sEMG sensor was processed through an input module (Bagnoli^{TM} Desktop, DELSYS, MA, USA) and a main amplifier (Bagnoli^{TM} Desktop, DELSYS, MA, USA) with a gain of 10k. In addition, the main amplifier filtered the signal to a bandwidth between 20 Hz and 450 Hz and checked for excessive amounts of line interference as well as channel clipping due to over-amplified signals. Finally, the processed load cell signal and the sEMG signal were collected by a data acquisition board (QPIDe Board, Quanser, Canada) through analog input channels. TA muscle contraction was imaged using a commercial linear array transducer (L7.5SC, 6.4 MHz center frequency) that is connected to a US imaging scanner (Prodigy, S-Sharp, Taiwan).

Signals from sEMG, US imaging, and load cell were synchronously recorded in a real-time system implemented in Matlab/Simulink (R2012b, MathWorks, MA, USA) controlled by trigger signals. The load cell and sEMG signals were sampled at 1000 Hz. US B-mode images on a targeted TA muscle region were acquired at a frame rate of 20 Hz. Supposed the time instants for collecting load cell and sEMG

signals are set as t_k, and for collecting US images are set as $t_{\bar{k}}$, then $\triangle t_k = t_{k+1} - t_k = 0.001$ s and $\triangle t_{\bar{k}} = t_{\bar{k}+1} - t_{\bar{k}} = 0.05$ s. For the sEMG signal, moving root mean square (MRMS) [41] [42] is given as

$$x_1(t_k) = rms\{l(t_k)\} = \left(\frac{1}{T}\sum_{t_k}^{t_k+T\triangle t_k} l^2(t_k)\right)^{1/2} \tag{13}$$

where $T\triangle t_k \in \mathbb{R}^+$ represents the length of the moving window, $l(t_k)$ and $x_1(t_k)$ represent the amplitude of sEMG signal and the sEMG MRMS at 1000 Hz, respectively.

Then the normalization of sEMG MRMS is represented by

$$n_1(t_k) = \frac{x_1(t_k) - x_{1\,\min}}{x_{1\,\max} - x_{1\,\min}} \tag{14}$$

where $x_{1\,\min}$ and $x_{1\,\max}$ denote the minimum value of MRMS in the corresponding trial and maximum value of MRMS at MVIC, respectively. As mentioned before, $\triangle t_{\bar{k}} = 50\triangle t_k$, to match the low sampling rate of US images, the sEMG-induced muscle activation $a_1(t_k)$ in (2) is downsampled to get $a_1(t_{\bar{k}}) = a_1(50t_k)$.

For the US images during the same contraction period, as shown in Fig. 1 (a), the PA φ was defined as the angle between the most clearly visualized fascicle and its insertion to the deep aponeurosis surface or baseline. To derive the musculoskeletal parameters including φ, l_m, and l_o of each US imaging frame, the commercial Matlab GUI software (R2017a, MathWorks, MA, USA) called *Muscle Fascicle Tracking* was utilized, whose algorithm is detailed in [35], [36].

Once the PA is derived from US images by using the GUI, the normalization of PA is given as

$$N_2(t_{\bar{k}}) = \frac{x_2(t_{\bar{k}}) - x_{2\,\min}}{x_{2\,\max} - x_{2\,\min}} \tag{15}$$

where $x_2(t_{\bar{k}})$ denotes PA at frame rate of 20 Hz, and $x_{2\,\min}$ and $x_{2\,\max}$ denote the minimum value of PA in the corresponding trial and maximum value of PA at MVIC, respectively. Therefore, the discrete form of the synthesized muscle activation in (4) is given as

$$a(\triangle t_{\bar{k}}) = \delta a_1(50\triangle t_k) + (1-\delta)a_2(\triangle t_{\bar{k}}).$$

IV. Results and Discussions

A. Results of Pre-processing

To simplify the notation of different scenarios on these 4 participants, the abbreviations such as A1S0, A1S10, and A1S-10 are used throughout the paper, which means the scenario 0°, 10°, and -10° on the first participant, respectively. Fig. 3 (a) shows the measurements synchronously collected by the data acquisition board and US machine in one typical trial for A1S0, including the force on the load cell (at 1000 Hz), sEMG of the TA muscle (at 1000 Hz), and PA calculated from US images (at 20 Hz). There are two dorsiflexion cycles in this trial with different elapsed times, which is likely due to the difficulty for participants to generate exactly repeated motion. The normalization of sEMG MRMS and PA from this typical trial are also shown in Fig. 3 (b). Correlation analysis is performed to reveal the preliminary relationships between

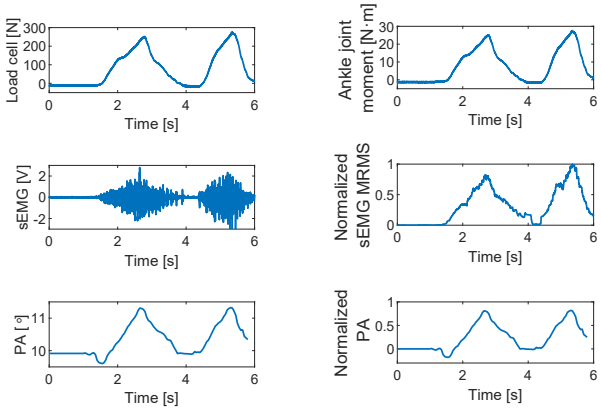

(a) (b)

Figure 3: (a) Original measurements of load cell, sEMG and PA of trial 1 during A1S0. During one contraction cycle, the force on load cell and PA are increasing monotonically, as well as the magnitude and density of sEMG are both increasing. (b) Computed ankle joint moment, as well as the normalization of sEMG MRMS and PA.

Table I: Correlation analysis results under 7 scenarios on A1 between ankle joint moment and normalized sEMG MRMS, between ankle joint moment and normalized PA

Variables	Moment and sEMG MRMS		Moment and PA	
Correlation analysis	CC	P	CC	P
S0	0.8145	<0.0001	0.8708	<0.0001
S5	0.9724	<0.0001	0.8106	<0.0001
S10	0.7939	<0.0001	0.8575	<0.0001
S15	0.9665	<0.0001	0.8281	<0.0001
S-5	0.9793	<0.0001	0.8823	<0.0001
S-10	0.9747	<0.0001	0.8347	<0.0001
S-15	0.9831	<0.0001	0.8186	<0.0001

moment and sEMG MRMS, as well as between moment and PA. The results under 7 scenarios on the first participant are listed in Table I, where CC means the averaged correlation coefficient for the three trials under each scenario, and P means the averaged p-value for testing the null hypothesis. The results reveal that the corresponding correlation between the ankle moment and sEMG is significant, and the corresponding correlation between the ankle moment and PA is also significant.

The time delay between sEMG and load cell is defined as EMD, which is varying across different participants. It is assumed that the EMD value remains same per participant across scenarios. The averaged EMD value from all trials during all scenarios on each participant are listed in Table II, which are used in the neural activation in (1). The MRMS can smooth the original sEMG singles, which appears the similar functionality as a low-pass filter. However, the length of the moving window $T\triangle t_k$ in (13) affects both the smoothness and information integrity of sEMG signal. To make a trade-off, $T\triangle t_k$ is set as 0.2 second throughout all experiments.

Table II: Averaged EMD for all scenarios on each participant

Participant	A1	A2	A3	A4
Averaged EMD (ms)	40	45	42	48

B. Results of System Identification

The focus in this work is to predict ankle dorsiflexion moment during the VC rising period, which ranges from no contraction to MVIC, such as between 1.40 s and 2.78 s in Fig. 3. During A1S0, there are two more repeated trials and the pre-processed results are similar to Fig. 3. In total, there are 84 trials in different scenarios on 4 participants. There are three different categories that calculate muscle activation, which was defined in (4). If $\delta = 1$, it is treated as sEMG-induced muscle activation, if $\delta = 0$, it is treated as PA-induced muscle activation, and if $0 < \delta < 1$, it is treated as synthesis-induced muscle activation. The three categories of muscle activation correspond to three kinds of HNM with unknown parameters. To derive these parameters and perform HNM-based dorsiflexion moment prediction, system identification (SI) is performed. The schematic of the proposed HNM-based SI is presented in Fig. 4, where the synthesized muscle activation depends on both sEMG signal and US images. Five unknown parameters (δ, A, c_1, c_2 and b_1) need to be identified in the SI with synthesized muscle activation, while four unknown parameters (A, c_1, c_2 and b_1) in the other two situations. In each trial, the Matlab function $lqscurvefit$ is utilized to determine the unknown parameters for three HNMs with same initial values, which is also defined as the training.

Data collected during the first VC rising period in each trial as shown in Fig. 3 (b) between 1.40 s and 2.78 s are used for training step, and the data in the remaining second VC rising period are used for prediction. Corresponding to the trial in Fig. 3, the training results based on three kinds of HNMs are presented in Fig. 5, where red solid line, deep blue dashed line, green center line, and blue dotted line represent the moments from measurement (M_l), synthesis-induced training (M_{both}), sole sEMG-induced training (M_{sEMG}), and sole PA-induced training (M_{PA}), respectively. Among three training methods, the tracking performance of M_{both} is the best. To quantitatively evaluate the performance of three training methods for repeated trials during A1S0, root mean square values (RMS) of errors (errors between M_{both} and M_l, M_{sEMG} and M_l, M_{PA} and M_l are represented as e_1, e_2 and e_3) and R-squared values (R^2) between trained moment and measured moment are calculated. RMS of e_1, e_2 and e_3 values are 1.21±0.19 N·m (mean±standard deviation), 1.61±0.40 N·m, and 3.05±0.43 N·m, respectively, and R^2 values are 0.978±0.007, 0.963±0.018, and 0.902±0.026, respectively. These preliminary training results indicate that, potentially, the synthesis-induced HNM can provide better ankle moment predictions.

Without loss of generality, the main purpose of these three categories of SI is to retrieve the unknown parameters based on least mean square (LMS) criterion. During each scenario for each participant, there are three VC rising periods utilized to get three groups of unknown parameters for HNMs with different muscle activation categories. The averaged value of each parameter in those three groups is computed and regarded as the unique identified parameters during that scenario. Table III (see Appendix) contains the unique parameters for HNM based on synthesized muscle activation during each scenario on 4 participants, while Table IV (see Appendix) and Table V (see Appendix) contain the unique parameters for HNM based on sEMG-induced muscle activation and PA-induced muscle activation, respectively.

In Table V, all the shape coefficients A are all equal to 0.080 in every scenario on every participant, however, the rest of the results from the parameter identification show a variance in a same parameter across scenarios on the same participant. For example, there is no constant allocation coefficient between the sEMG-induced and PA-induced muscle activation across 7 isometric dorsiflexion scenarios for each participant as listed in Table III. In addition, the identified values of c_2 are fluctuating around 1 for all scenarios, and apart from A1S5, A1S10, A1S15 and A1S-5, the identified values of c_1 are all less than 1. All these HNM parameters are used for the moment prediction as described in the next section.

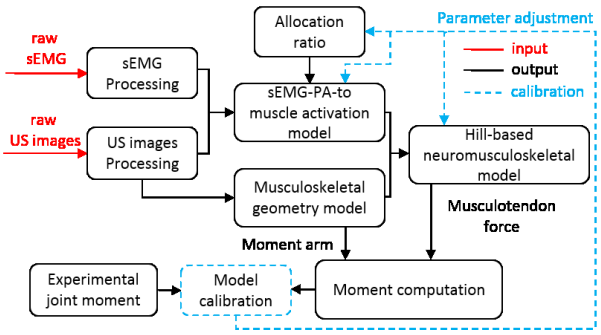

Figure 4: Schematic of the HNM-based system identification methodology. The synthesized muscle activation combines both sEMG signal and US images. Neural activation are derived from sEMG MRMS, which composes one part of muscle activation, and the other part of muscle activation comes from the normalized PA from US images.

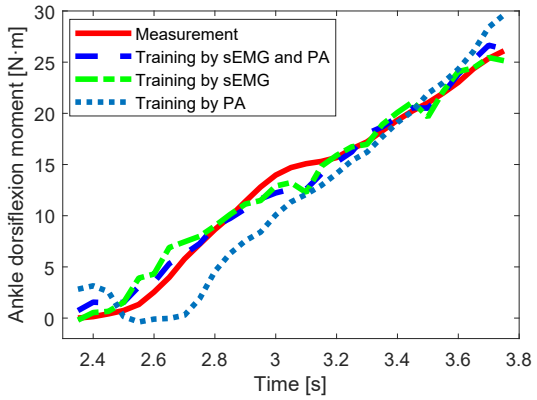

Figure 5: Training results based on HNM-based approach with synthesized muscle activation, sole sEMG-induced muscle activation, and sole PA-induced muscle activation of trial 1 during A1S0.

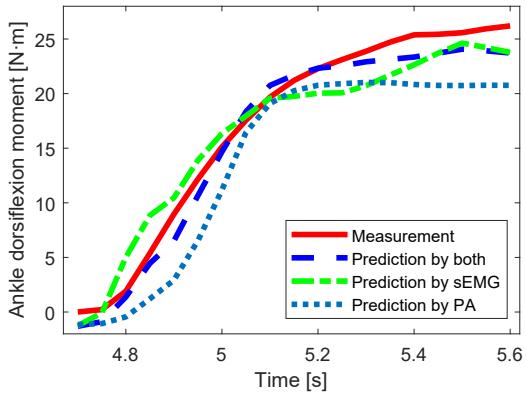

Figure 6: Prediction results by using the HNM-based approach with the synthesis-induced, only sEMG-induced, and only PA-induced muscle activation in trial 2 of A4S5.

C. Results of Model-based Prediction

All the parameters identification are off-line and it is assumed that the unknown parameters remain constant in each corresponding scenario for prediction due to the autonomous HNM system. Three repeated dorsiflexion cycles in each scenario on each participant (the second VC rising period as shown in Fig. 3) are utilized to validate the effectiveness of the proposed HNM-based moment prediction method. For example, the prediction results of one typical trial during A4S5 are shown in Fig. 6, where red solid line, deep blue dashed line, green center line and blue dotted line represent the moment from measurement (M_l), synthesis-induced prediction (M_{both}), sole sEMG-induced prediction (M_{sEMG}) and sole PA-induced prediction (M_{PA}), respectively. Obviously, synthesis-induced prediction is the best approach to track the measured joint moment. During A4S5, the RMS of e_1, e_2 and e_3 are 1.21$\pm$0.21 N·m, 2.29$\pm$0.38 N·m and 2.89$\pm$1.04 N·m, respectively, as well as the R^2 between the predicted moment and measured moment are 0.979$\pm$0.016, 0.933$\pm$0.031 and 0.964$\pm$0.027, respectively.

For every scenario on 4 participants from A1S0 to A4S-15, the same quantitative evaluation is performed as mentioned above. Furthermore, to investigate the generalization of the proposed prediction method, validations across scenarios (VAS) and validations across participants (VAP) are performed. VAS analysis potentially shows that prediction can also be applied in non-isometric ankle dorsiflexion and VAP analysis potentially shows the prediction's generalizability or applicability on different human participants.

The RMS values of e_1, e_2, and e_3 in VAS are shown in Fig. 7 (a), and R^2 between predicted and measured ankle moment in VAS are shown in Fig. 7 (b). Similarly, the RMS values and R^2 values in VAP are shown in Fig. 8 (a) and Fig. 8 (b), respectively. The Kolmogorov-Smirnov test is used to determine if the RMS data and R^2 data are normally distributed data sets in these two validation types. The test shows that the RMS data and R^2 data sets are normally distributed. In VAS, Fig. 7 (a) shows that the averaged RMS of e_1 is smaller than that of e_2 or e_3. Furthermore, to determine whether there exists a significant difference between RMS of e_1 and RMS of e_2 or e_3, one-way analysis of variance (ANOVA) and Tukey's honestly significant difference test (Tukey's HSD) are used. As shown in Fig. 7 (a), apart from the comparison between RMS of e_1 and RMS of e_2 on participant A4, all other comparisons show significant difference between RMS of e_1 and RMS of e_2, as well as between RMS of e_1 and RMS of e_3, which implies the HNM with synthesized muscle activation can significantly reduce the RMS of errors between the predicted and measured moment than sole sEMG-induced muscle activation or sole PA-induced muscle activation. Fig. 7 (b) shows that the averaged R^2 of M_{both}-M_l is higher than that of M_{sEMG}-M_l or M_{PA}-M_l. Furthermore, apart from the comparison between R^2 of M_{both}-M_l and R^2 of M_{PA}-M_l on participant A3, all other comparisons show significant difference between R^2 of M_{both}-M_l and R^2 of M_{sEMG}-M_l, as well as between R^2 of M_{both}-M_l and R^2 of M_{PA}-M_l, which implies the HNM with synthesized muscle activation can also significantly improve the R^2 between the predicted and measured moment than sole sEMG-induced muscle activation or sole PA-induced muscle activation.

In VAP, without loss of generality, Fig. 8 (a) shows that the averaged RMS of e_1 is smaller than that of e_2 or e_3 except for S-15, and Fig. 8 (b) shows that the averaged R^2 of M_{both}-M_l is higher than that of M_{sEMG}-M_l or M_{PA}-M_l. Furthermore, the results in Fig. 8 (a) show there is no significant difference between RMS of e_1 and RMS of e_3 during S0, between RMS of e_1 and RMS of e_2 during S-10 and S-15. The results in Fig. 8 (b) show there is no significant difference between R^2 of M_{both}-M_l and R^2 of M_{sEMG}-M_l during S-10 and S-15, between R^2 of M_{both}-M_l and R^2 of M_{PA}-M_l during S0 and S-5. By comparing RMS of e_1 and RMS of e_2 or e_3, the rates of significant RMS reduction by employing synthesis-induced muscle activation for prediction are 71.43 % (5 out of 7 scenarios) and 85.71 % (6 out of 7 scenarios). Similarly by comparing R^2 of M_{both}-M_l and R^2 of M_{sEMG}-M_l or M_{PA}-M_l, both rates of the significant R^2 improvement are 71.43 % (5 out of 7 scenarios).

The analysis of prediction results through VAS and VAP reveals a strong potential that the proposed HNM-based ankle dorsiflexion moment prediction method, by combining sEMG and PA, would reduce the RMS of prediction error and improve the R^2 between the prediction and measurement.

D. Discussion

In the current study, an sEMG and PA synthesis-induced HNM was developed to predict the joint moment during voluntary isometric ankle dorsiflexion. The architectural parameters from US images were utilized to formulate the participant-specific musculoskeletal geometry model. The sEMG was utilized to build the neural activation model contributing to part of the muscle activation model and PA was utilized to build the other part of the muscle activation model. By adjusting eachcomponents' allocation coefficients, three kinds of SI were used to identify unknown parameters in different HNMs individually. By implementing the identified parameters in each HNM (i.e., different muscle activation

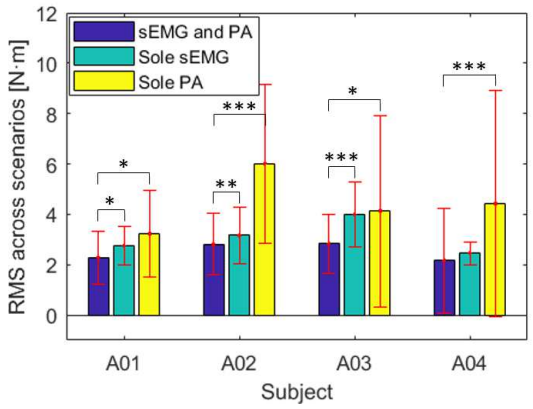

(a)

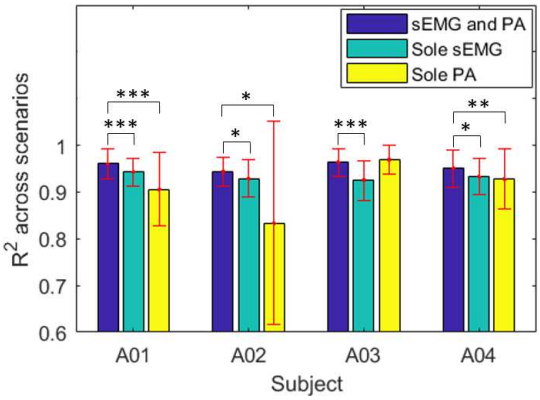

(b)

Figure 7: Prediction performance based on HNM with three kinds of muscle activation through VAS. (a) RMS of e_1, e_2 and e_3 on each participant. (b) R^2 between the predicted and measured ankle joint moment on each participant. * represents the significant difference level is at p<0.05, ** represents the significant difference level is at p<0.01, and *** represents the significant difference level is at p<0.001.

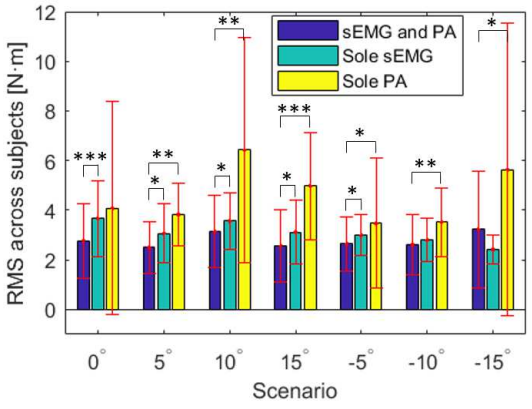

(a)

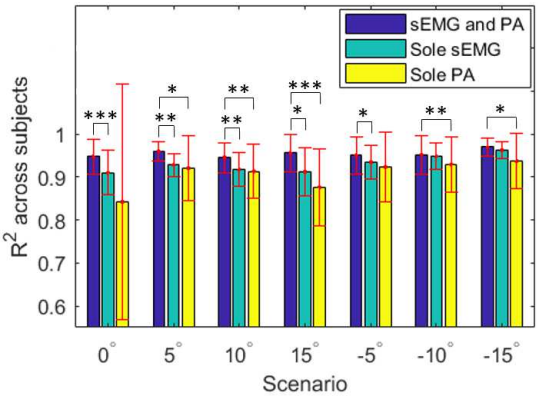

(b)

Figure 8: Performance comparison based on HNM with three kinds of muscle activation through VAP. (a) RMS between the predicted and measured ankle joint moment corresponding to different muscle activation sources. (b) R^2 between the predicted and measured ankle joint moment corresponding to different muscle activation sources.

types), the dorsiflexion moment prediction performance for each HNM was compared . The feasibility and reliability of the sEMG and PA synthesis-induced HNM were evaluated through VAS and VAP analysis. The experimental results showed that the synthesis-induced HNM can provide higher dorsiflexion moment prediction accuracy than using sole sEMG or sole PA extracted from US images in the HNM.

The idea that establishes an HNM that uses structural variables from US images to predict muscle force or joint moment has also been studied in recent research work. Dick et. al [22] compared the human gastrocnemius forces predicted by Hill-type models with forces estimated from US-based measures of tendon length change and stiffness during a cycling scenario. However, only sEMG was used to derive muscle activation for both slow and fast muscle fibers. In [43], a geometrical model and a Hill-type musculotendon model were combined to predict an individual muscle force. A linear envelope method was used to obtain muscle activation level from EMG. Recently, traditional HNM-based force or torque prediction based on sEMG signals have been studied in [27], [28]. However, those studies only considered the EMG-induced activation factor in the muscle activation dynamics. Few studies have incorporated the architectural parameters of the targeted muscle to the muscle contraction in an HNM. In addition, the approximated offline physiological parameters from OpenSim software can hardly reflect the real-time neuromuscular conditions of an individual participant. Furthermore, the subjective real-time implementation of the HNM is significantly limited due to the virtual and asynchronous physiological parameters of the targeted muscle.

The merits in this work include two aspects. The first merit is that we introduce variables from US images to establish the HNM, where the muscle activation is designed as the weighted summation of sEMG-induced activation and PA-induced activation. The second merit is that the calculation of fascicle length, fascicle velocity, and PA are based on the optical flow tracking algorithm, which provides the potentials for real-time implementation. The proposed HNM-based dorsiflexion moment prediction approach provides higher reliability and accuracy for human movement intent detection. Based on the human movement intent, advanced control strategies

like "assist-as-need" control scheme [1]–[3] can be developed successfully for state-of-the-art neurorehabilitation techniques, including powered exoskeletons [44]–[46] and functional electrical stimulation (FES) [47], [48]. These two technologies aim to induce neural reorganization through therapeutic exercises [42] are essential to improve weakened function or dysfunction of ankle dorsiflexion, like drop foot that may result from spinal cord injury (SCI) [49] or cerebral vascular accidents [50].

"Why the HNM-based approach that combines an sEMG signal and a US imaging signal predicts ankle dorsiflexion moment with a higher accuracy? We propose that both signals provide complementary information. An sEMG signal and a US imaging signal are both indirect measures of descending neural signals from the spinal cord. sEMG signals measure electric potentials generated by muscle cells when they are neurally activated. The amplitude of a filtered and rectified sEMG signal linearly correlates with the number of firing neurons, which offers a physical measurement of the micro-physiological response [51]. While, US imaging signals show visualized information of the macro-physiological response [52] of a targeted muscle caused by a neural firing. Thus, sEMG signals and US-imaging derived signals provide the information from an electrical aspect and a mechanical aspect, respectively, in response to the same physiological stimulus. Secondly, considering the individual shortcomings of the sEMG signal and the US imaging signal, which are mentioned in the introduction section, their combination can 1) mitigate any cross-talking effect from neighboring sEMG signals, 2) lower the PA calculation drift caused by the accumulated fascicle orientation using an optimal flow tracking algorithm. Therefore, the combination of the micro-related and macro-related information results in a better ankle moment prediction performance.

However, there exist some limitations in the current work. The accuracy of geometry parameters extraction from US images depends on the effectiveness of $Muscle\ Fascicle\ Tracking$ software and the US imaging frame rate. If the frame rate is too high, the low signal-to-noise ratio (SNR) between consecutive frames can deteriorate the fascicle tracking performance. However, if the frame rate is too low, even though SNR is high, the large deformation between successive US images result in a low correlation. Therefore some obvious features of the fascicle in current frame might not fully remain in next frame, which also negatively affects the fascicle tracking performance. As shown in Fig. 5, theoretically, with the increasing of VC, the moment in PA-induced training should increase monotonically. However, it decreases from 2.4 s to 2.6 s. This inaccuracy affects severely on both synthesis-induced and PA-induced HNM-based moment prediction than sEMG-induced moment prediction. The unknown parameters in HNM on the same participant may be time varying for different trials in each scenario, but the recognition of this change is still an open research area, which is not included here. Furthermore, the current study is limited to unipennate muscles or to a bipennate TA, provided region of interest (ROI) is focused to a smaller region where muscle fascicles have same orientation. The study does not provide methods to compute PA from multipennate and circumpennate muscles.

V. Conclusion

To non-invasively predict ankle dorsiflexion moment, a modified version of HNM was proposed by combing sEMG signal and PA extracted from US images. This model was compared with HNMs with sole sEMG-induced muscle activation or sole PA-induced muscle activation. The unknown parameters from the three HNMs were identified based on nonlinear least squares method through synchronously recorded load cell, sEMG, and PA signals. The HNM-based ankle dorsiflexion moment prediction was performed by using the identified parameters and new recorded data sets. Both VAS and VAP verified the effectiveness and reliability of this model-based moment prediction method. The statistical analysis of VAP showed that RMS of prediction errors in sole sEMG-induced model and sole PA-induced model were significantly reduced by 71.43 % (5 out of 7 scenarios) and 85.71 % (6 out of 7 scenarios) compared to synthesized model, respectively, and R^2 between predicted and measured ankle joint moment in sole sEMG-induced model and sole PA-induced model were both significantly improved by 71.43 % (5 out of 7 scenarios). These findings provide a more accurate approach for detecting human movement intention of lower limbs, which is beneficial for developing robot-assisted or FES-assisted lower limb motor function recovery based on the assist-as-needed principle.

Appendix

The parameters from system identification based on three kinds of HNMs are given in the supplementary document.

References

[1] M. Bortole, A. Venkatakrishnan, F. Zhu, J. C. Moreno, G. E. Francisco, J. L. Pons, and J. L. Contreras-Vidal, "The H2 robotic exoskeleton for gait rehabilitation after stroke: early findings from a clinical study," *J. Neuroeng. Rehabil.*, vol. 12, no. 1, p. 54, 2015.

[2] A. U. Pehlivan, D. P. Losey, and M. K. OMalley, "Minimal Assist-as-Needed Controller for Upper Limb Robotic Rehabilitation," *IEEE Trans. Robot.*, vol. 32, no. 1, pp. 113–124, 2016.

[3] M. Shahbazi, S. F. Atashzar, M. Tavakoli, and R. V. Patel, "Robotics-Assisted Mirror Rehabilitation Therapy: A Therapist-in-the-Loop Assist-as-Needed Architecture," *IEEE/ASME Trans. Mechatron.*, vol. 21, no. 4, pp. 1954–1965, 2016.

[4] J. Sun, Z. Guo, Y. Zhang, X. Xiao, and J. Tan, "A Novel Design of Serial Variable Stiffness Actuator Based on an Archimedean Spiral Relocation Mechanism," *IEEE ASME Trans. Mechatron.*, vol. 23, no. 5, pp. 2121–2131, 2018.

[5] Q. Zhang, D. Sun, W. Qian, X. Xiao, and Z. Guo, "Modeling and Control of a Cable-Driven Rotary Series Elastic Actuator for Upper Limb Rehabilitation Robot," *Front. Neurorobot.*, Submitted, 2019.

[6] S. Wang, L. Wang, C. Meijneke, E. van Asseldonk, T. Hoellinger, G. Cheron, Y. Ivanenko, V. La Scaleia, F. Sylos-Labini, M. Molinari, F. Tamburella, I. Pisotta, F. Thorsteinsson, M. Ilzkovitz, J. Gancet, Y. Nevatia, R. Hauffe, F. Zanow, and H. van der Kooij, "Design and Control of the MINDWALKER Exoskeleton," *IEEE Trans. Neural Syst. Rehabil. Eng.*, vol. 23, no. 2, pp. 277–286, 2015.

[7] D. Zanotto, Y. Akiyama, P. Stegall, and S. K. Agrawal, "Knee Joint Misalignment in Exoskeletons for the Lower Extremities: Effects on User's Gait," *IEEE Tran. Robot.*, vol. 31, no. 4, pp. 978–987, 2015.

[8] R. Gopura, D. Bandara, K. Kiguchi, and G. Mann, "Developments in hardware systems of active upper-limb exoskeleton robots: A review," *Rob. Auton. Syst.*, vol. 75, pp. 203–220, 2016.

[9] He Huang, Ping Zhou, Guanglin Li, and T. Kuiken, "An Analysis of EMG Electrode Configuration for Targeted Muscle Reinnervation Based Neural Machine Interface," *IEEE Trans. Neural Syst. Rehabil. Eng.*, vol. 16, no. 1, pp. 37–45, 2008.

[10] M. Sartori, D. G. Llyod, and D. Farina, "Neural data-driven musculoskeletal modeling for personalized neurorehabilitation technologies," *IEEE Trans. Biomed. Eng.*, vol. 63, no. 5, pp. 879–893, 2016.

[11] J.-Y. Guo, Y.-P. Zheng, L. P. Kenney, A. Bowen, D. Howard, and J. J. Canderle, "A Comparative Evaluation of Sonomyography, Electromyography, Force, and Wrist Angle in a Discrete Tracking Task," *Ultrasound Med. Biol.*, vol. 37, no. 6, pp. 884–891, 2011.

[12] J. Shi, Y. P. Zheng, Q. H. Huang, and X. Chen, "Continuous monitoring of sonomyography, electromyography and torque generated by normal upper arm muscles during isometric contraction: Sonomyography assessment for arm muscles," *IEEE Trans. Biomed. Eng.*, vol. 55, no. 3, pp. 1191–1198, 2008.

[13] Q. Zhang, Z. Sheng, F. Moore-Clingenpeel, K. Kim, and N. Sharma, "Ankle dorsiflexion strength monitoring by combining sonomyography and electromyography," in *Proc Int. Conf. Rehabil. Robot.* IEEE, 2019, pp. 240–245.

[14] J.-Y. Guo, Y.-P. Zheng, H.-B. Xie, and X. Chen, "Continuous monitoring of electromyography (EMG), mechanomyography (MMG), sonomyography (SMG) and torque output during ramp and step isometric contractions," *Med. Eng. Phys.*, vol. 32, no. 9, pp. 1032–1042, 2010.

[15] P. Hodges, L. Pengel, R. Herbert, and S. Gandevia, "Measurement of muscle contraction with ultrasound imaging," *Muscle & Nerve*, vol. 27, no. 6, pp. 682–692, 2003.

[16] H. H. Savelberg and W. Herzog, "Prediction of dynamic tendon forces from electromyographic signals: An artificial neural network approach," *J. Neurosci. Methods*, vol. 78, no. 1-2, pp. 65–74, 1997.

[17] M. M. Liu, W. Herzog, and H. H. Savelberg, "Dynamic muscle force predictions from EMG: an artificial neural network approach," *J. Electromyogr. Kinesiol.*, vol. 9, no. 6, pp. 391–400, 1999.

[18] F. Sepulveda, D. M. Wells, and C. L. Vaughan, "A neural network representation of electromyography and joint dynamics in human gait," *J. Biomech.*, vol. 26, no. 2, pp. 101–109, 1993.

[19] D. L. Crouch, L. Pan, W. Filer, J. W. Stallings, and H. Huang, "Comparing Surface and Intramuscular Electromyography for Simultaneous and Proportional Control Based on a Musculoskeletal Model: A Pilot Study," *IEEE Trans. Neural Syst. Rehabil. Eng.*, vol. 26, no. 9, pp. 1735–1744, 2018.

[20] D. Ao, R. Song, and J. Gao, "Movement Performance of Human-Robot Cooperation Control Based on EMG-Driven Hill-Type and Proportional Models for an Ankle Power-Assist Exoskeleton Robot," *IEEE Trans. Neural Syst. Rehabil. Eng.*, vol. 25, no. 8, pp. 1125–1134, 2017.

[21] S. Yao, Y. Zhuang, Z. Li, and R. Song, "Adaptive admittance control for an ankle exoskeleton using an EMG-driven musculoskeletal model," *Front. Neurorobot.*, vol. 12, 2018.

[22] T. J. M. Dick, A. A. Biewener, and J. M. Wakeling, "Comparison of human gastrocnemius forces predicted by Hill-type muscle models and estimated from ultrasound images," *J. Exp. Biol.*, vol. 220, no. 9, pp. 1643–1653, 2017.

[23] E. K. Chadwick, D. Blana, R. F. Kirsch, and A. J. Van Den Bogert, "Real-time simulation of three-dimensional shoulder girdle and arm dynamics," *IEEE Trans. Biomed. Eng.*, vol. 61, no. 7, pp. 1947–1956, 2014.

[24] D. Farina and F. Negro, "Accessing the Neural Drive to Muscle and Translation to Neurorehabilitation Technologies," *IEEE Rev. Biomed. Eng.*, vol. 5, pp. 3–14, 2012.

[25] D. Kumar, K. S. Rudolph, and K. T. Manal, "EMG-driven modeling approach to muscle force and joint load estimations: Case study in knee osteoarthritis," *J. Orthop. Res.*, vol. 30, no. 3, pp. 377–383, 2012.

[26] T. F. Besier, M. Fredericson, G. E. Gold, G. S. Beaupré, and S. L. Delp, "Knee muscle forces during walking and running in patellofemoral pain patients and pain-free controls," *J. Biomech.*, vol. 42, no. 7, pp. 898–905, 2009.

[27] M. Sartori, M. Reggiani, E. Pagello, and D. G. Lloyd, "Modeling the Human Knee for Assistive Technologies," *IEEE Trans. Biomed. Eng.*, vol. 59, no. 9, pp. 2642–2649, 2012.

[28] M. Sartori, M. Reggiani, D. Farina, and D. G. Lloyd, "EMG-Driven Forward-Dynamic Estimation of Muscle Force and Joint Moment about Multiple Degrees of Freedom in the Human Lower Extremity," *PLoS ONE*, vol. 7, no. 12, p. e52618, 2012.

[29] P. Gerus, M. Sartori, T. F. Besier, B. J. Fregly, S. L. Delp, S. A. Banks, M. G. Pandy, D. D. D'Lima, and D. G. Lloyd, "Subject-specific knee joint geometry improves predictions of medial tibiofemoral contact forces," *J. Biomech.*, vol. 46, no. 16, pp. 2778–2786, 2013.

[30] C. Winby, D. Lloyd, T. Besier, and T. Kirk, "Muscle and external load contribution to knee joint contact loads during normal gait," *J. Biomech.*, vol. 42, no. 14, pp. 2294–2300, 2009.

[31] S. Pfeifer, H. Vallery, M. Hardegger, R. Riener, and E. J. Perreault, "Model-Based Estimation of Knee Stiffness," *IEEE Trans. Biomed. Eng.*, vol. 59, no. 9, pp. 2604–2612, 2012.

[32] M. Sartori, M. Maculan, C. Pizzolato, M. Reggiani, and D. Farina, "Modeling and simulating the neuromuscular mechanisms regulating ankle and knee joint stiffness during human locomotion," *J. Neurophysiol.*, vol. 114, no. 4, pp. 2509–2527, 2015.

[33] R. S. Barrett, T. F. Besier, and D. G. Lloyd, "Individual muscle contributions to the swing phase of gait: An EMG-based forward dynamics modelling approach," *Simul. Model. Practice Theory*, vol. 15, no. 9, pp. 1146–1155, 2007.

[34] T. Desplenter, A. Trejos, T. Desplenter, and A. L. Trejos, "Evaluating Muscle Activation Models for Elbow Motion Estimation," *Sensors*, vol. 18, no. 4, 2018.

[35] N. J. Cronin, C. P. Carty, R. S. Barrett, and G. Lichtwark, "Automatic tracking of medial gastrocnemius fascicle length during human locomotion," *J. Appl. Biomech.*, vol. 111, no. 5, pp. 1491–1496, 2011.

[36] J. G. Gillett, R. S. Barrett, and G. A. Lichtwark, "Reliability and accuracy of an automated tracking algorithm to measure controlled passive and active muscle fascicle length changes from ultrasound," *Comput. Methods Biomech. Biomed. Engin.*, vol. 16, no. 6, pp. 678–687, 2013.

[37] D. G. Lloyd and T. F. Besier, "An EMG-driven musculoskeletal model to estimate muscle forces and knee joint moments in vivo," *J. Biomech.*, vol. 36, no. 6, pp. 765–776, 2003.

[38] K. Manal and T. S. Buchanan, "A one-parameter neural activation to muscle activation model: estimating isometric joint moments from electromyograms," *J. Biomech.*, vol. 36, no. 8, pp. 1197–1202, 2003.

[39] R. Riener and T. Fuhr, "Patient-driven control of FES-supported standing up: A simulation study," *IEEE Trans. Rehabil. Eng.*, vol. 6, pp. 113–124, 1998.

[40] H. Hatze, "A myocybernetic control model of skeletal muscle," *Biol. Cybern.*, vol. 25, no. 2, pp. 103–119, 1977.

[41] K. Watanabe and H. Akima, "Normalized EMG to normalized torque relationship of vastus intermedius muscle during isometric knee extension," *Eur. J. Appl. Physiol.*, vol. 106, no. 5, pp. 665–673, 2009.

[42] Q. Zhang, Z. Sheng, K. Kim, and N. Sharma, "Observer Design for a Nonlinear Neuromuscular System with Multi-rate Sampled and Delayed Output Measurements," in *Proc. Am. Control Conf.* IEEE, 2019, pp. 872–877.

[43] L. Li, K. Tong, X. Hu, L. Hung, and T. Koo, "Incorporating ultrasound-measured musculotendon parameters to subject-specific emg-driven model to simulate voluntary elbow flexion for persons after stroke," *Clin. Biomech.*, vol. 24, no. 1, pp. 101–109, 2009.

[44] P.-C. Kao, C. L. Lewis, and D. P. Ferris, "Invariant ankle moment patterns when walking with and without a robotic ankle exoskeleton," *J. Biomech.*, vol. 43, no. 2, pp. 203–209, 2010.

[45] G. Chen, C. K. Chan, Z. Guo, and H. Yu, "A Review of Lower Extremity Assistive Robotic Exoskeletons in Rehabilitation Therapy," *Crit. Rev. Biomed. Eng.*, vol. 41, no. 4-5, pp. 343–363, 2013.

[46] R. Jiménez-Fabián and O. Verlinden, "Review of control algorithms for robotic ankle systems in lower-limb orthoses, prostheses, and exoskeletons," *Med. Eng. Phys.*, vol. 34, no. 4, pp. 397–408, 2012.

[47] R. van Swigchem, H. J. van Duijnhoven, J. den Boer, A. C. Geurts, and V. Weerdesteyn, "Effect of Peroneal Electrical Stimulation Versus an Ankle-Foot Orthosis on Obstacle Avoidance Ability in People With Stroke-Related Foot Drop," *Phys. Ther.*, vol. 92, no. 3, pp. 398–406, 2012.

[48] P. M. Kluding, K. Dunning, M. W. O'Dell, S. S. Wu, J. Ginosian, J. Feld, and K. McBride, "Foot Drop Stimulation Versus Ankle Foot Orthosis After Stroke," *Stroke*, vol. 44, no. 6, pp. 1660–1669, 2013.

[49] R. B. Stein, M. Bélanger, G. Wheeler, M. Wieler, D. B. Popović, A. Prochazka, and L. A. Davis, "Electrical systems for improving locomotion after incomplete spinal cord injury: An assessment," *Arch. Phys. Med. Rehabil.*, vol. 74, no. 9, pp. 954–959, 1993.

[50] M. H. Granat, D. J. Maxwell, A. C. Ferguson, K. R. Lees, and J. C. Barbenet, "Peroneal stimulator: Evaluation for the correction of spastic drop foot in hemiplegia," *Arch. Phys. Med. Rehabil.*, vol. 77, no. 1, pp. 19–24, 1996.

[51] M. Barbero, R. Merletti, and A. Rainoldi, *Atlas of muscle innervation zones: understanding surface electromyography and its applications*. Springer Science & Business Media, 2012.

[52] P. Aagaard, J. L. Andersen, P. Dyhre-Poulsen, A.-M. Leffers, A. Wagner, S. P. Magnusson, J. Halkjær-Kristensen, and E. B. Simonsen, "A mechanism for increased contractile strength of human pennate muscle in response to strength training: changes in muscle architecture," *J. Physiol.*, vol. 534, no. 2, pp. 613–623, 2001.